ARTICLE

Chiral 2D organic-inorganic hybrid perovskites based upon L-histidine

Received 00th January 20xx,
Accepted 00th January 20xx

DOI: 10.1039/x0xx00000x

Valerii Y. Sirenko, [a] Olesia I. Kucheriv, [b] Elzbieta Gumienna-Kontecka, [b] Sergiu Shova, [c,d] and Il'ya A. Gural'ski *[a]

Novel chiral hybrid perovskites are highly demanded for various advanced applications such as spintronics, optoelectronics, photovoltaics etc. However, the scope of these new materials is still limited. Herein, we present new 2D hybrid perovskites based upon chiral α-amino acid L-histidine. The generalized formula of these new compounds can be denoted as $(L\text{-}HisH)_2PbBr_xI_{4-x}$ (where L-His = L-histidine; x = 4, 3, 2, 1, 0.4 and 0). All perovskites are characterized by a very similar structural motif that consists of corner-sharing lead halide octahedra arranged in one-layer thin inorganic slabs interleaved by organic layers established by L-histidinium(1+) cations. L-histidine provides a breaking of spatial parity of these perovskites that result in their non-centrosymmetric crystal structures. These compounds show a multiband absorption up to 590 nm for iodide perovskite. In addition, new compounds display pronounced single-peak photoluminescence, which finely blue shifts upon gradual substitution of iodine by bromine. New perovskites exhibit excellent thermal stability up to 490 K and 445 K for bromide and iodide compounds, respectively. These results show a perspective of L-histidine to produce novel and highly demanded chiral hybrid perovskites.

INTRODUCTION

Hybrid organic-inorganic perovskites have attracted significant research interest due to their promising application in optoelectronic,[1–5] spintronic[6] and photovoltaic[7–11] devices. Within a decade, the power conversion efficiency of perovskite solar cells has increased from 3.8% to a certified value of 25.7%,[12,13] the highest value among the solution-processable thin-film photovoltaics. Among the whole family of perovskites, three-dimensional (3D) halide perovskites have shown superior photovoltaic efficacy. This can be attributed to their unique optoelectronic properties, such as direct and suitable band gap,[14] extremely high absorption coefficient,[15] long charge carrier diffusion length,[16] excellent ambipolar charge carrier transport properties[17], high defect tolerance,[18] and possibility of solution-processing at low temperatures.[19] 3D organic-inorganic perovskites feature general formula ABX_3, where A is a monovalent cation, e.g., methylammonium ($CH_3NH_3^+$),[20,21] formamidinium ($HC(NH_2)_2$),[22,23] aziridinium ($CH_2(NH_2^+)CH_2$),[24] *etc.*[25–27], B is typically a metal cation and X is a halide anion such as I^-, Br^-, Cl^-.

Unfortunately, the main disadvantage of 3D halide perovskites is their poor stability towards environmental factors (humidity, heat, UV-radiation *etc*.).[28,29] The low stability of 3D perovskites urged many researches to seek alternatives based on more stable low dimensional perovskites.[30,31] Layered low-dimensional perovskites are also referred in literature as 2D perovskites and in virtue of their layered structure these compounds are characterized by extraordinary stability which stems from their low ion migration and water-resistant nature.[32] Besides, comparing to 3D perovskites, 2D perovskites offer unique structural flexibility, which provides the possibility to incorporate a great variety of functional organic cations to generate unique electronic and optical properties.[33–36] According to this, various chiral cations can be incorporated in the structure of 2D hybrid perovskites which renders them unique physical properties attributed to breaking of spatial parity, such as ferroelectricity,[37–40] nonlinear optical response,[41] circular dichroism,[42,43] circularly polarized photoluminescence[44] *etc.*

Interestingly, chiral low-dimensional perovskites can exhibit such phenomenon as ferroelectric-photovoltaic effect.[45] Such effect offers efficient pathways to accomplish charge separation in materials. The biggest difference between the photovoltaic effect in a ferroelectric material and that in a conventional semiconductor p-n junction is the magnitude of the electric field that separates the photogenerated electron-hole pair; the effective electric field in a ferroelectric material is

[a] *Department of Chemistry, Taras Shevchenko National University of Kyiv, Volodymyrska St. 64, 01601 Kyiv, Ukraine. E-mail: illia.guralskyi@univ.kiev.ua*
[b] *Faculty of Chemistry, University of Wrocław, F. Joliot-Curie 14, 50383 Wrocław, Poland.*
[c] *Ningbo University of Technology, No. 201, Fenghua Road, Ningbo City, Zhejiang, 315211, China.*
[d] *Department of Inorganic Polymers, ''Petru Poni'' Institute of Macromolecular Chemistry, 41A Aleea Gr. Ghica Voda, 700487 Iasi, Romania.*

† Footnotes relating to the title and/or authors should appear here.

Electronic Supplementary Information (ESI) available: experimental information, experimental/theoretical PXRD patterns, crystal data and refinement details. CCDC: 2207739 – 2207741. For ESI and crystallographic data in CIF or other electronic format, see DOI: 10.1039/x0xx00000x

around one order of magnitude higher than in a p-n junction. Thus, comparing to conventional photovoltaic materials, ferroelectric photovoltaic materials can produce voltages that are significantly higher than the bandgap. Besides, electric-field control over domain structure allows the photovoltaic effect in such materials to be reversed in polarity or turned off.

Among the whole scope of chiral organic molecules bearing amino group(s) chiral α-amino acids are the most interesting. Chiral α-amino acids are ubiquitous in nature and therefore they are easily accessible precursors. Previously, there were reports on hybrid halide perovskites incorporating chiral α-amino acids such as lysine,[46] ornithine[46], alanine[47] and proline[48]. However, examples of hybrid perovskites incorporating chiral α-amino acids are still rare.

Special attention is drawn to the chiral α-amino acid histidine, which is one of the essential amino acids. This molecule is interesting due its chirality and the side chain aromatic imidazolium ring which is small enough (r_{eff} = 2.58 Å)[49] to intrude in cuboctahedral cavities and facilitate the charge distribution between organic and inorganic part of hybrid perovskites. As was shown previously, incorporation of imidazole-ring-containing molecule into hybrid perovskites structures may result in narrowing of their band-gap. As an example, Li *et al.* reported a chiral hybrid perovskite $(C_5H_{11}N_3)SbI_5$ (where $C_5H_{11}N_3^{2+}$ is histammonium cation) which showed surprisingly low for Sb-containing perovskites band gap of ~1.79 eV which results in its black color.[50] Besides, temperature-dependent conductivity measurements confirmed the semiconductivity of this hybrid perovskite.

Previously, it was shown that hybrid perovskites incorporating organic molecules based on imidazole ring may be promising for photovoltaic application. Mao *et al.* proposed thin film solar cell based on 2D hybrid lead iodide perovskite $(HA)PbI_4$ (HA = histammonium cation) which shows maximum efficiency of 1.13%.[51] Another study showed thin film photovoltaic cell incorporating the same hybrid perovskite with power conversion efficiency of 1.83%.[52] It should be noted that this is the highest values obtained thus far for pure one-layer thick lead-iodide perovskites and more than 20 times higher than those obtained for materials based on more traditional cations such as phenylethylammonium (0.08%).[52]

Owing to the chirality of L- or D-histidine it can be used to produce noncentrosymmetric polar coordination compounds which are efficient for second-harmonic generation.[53,54] Recently, Tofanello et al. proposed novel strategy to provide magnetism to a 2D Ruddlesden-Popper perovskite using histidine molecules as a spacer, which could induce charge rebalancing at the interface of the inorganic layer. It was proposed that imidazole group, possibly assisted by the carboxyl group close to the vicinity of the terminal amine, is provoking charge rearrangement from Pb^{2+} to paramagnetic Pb^{3+} ions, resulting in a positive magnetic moment.[55]

According to all aforementioned achievements, histidine-based hybrid perovskites may be promising for various applications including photovoltaics, optoelectronics, spintronics *etc.* Unfortunately, the field of hybrid perovskites incorporating histidine molecule is still not explored.

Here we report a new chiral 2D organic-inorganic lead halide perovskites based on chiral α-amino acid L-histidine, namely $(L\text{-}HisH)_2PbBr_4$ (**Br_4**), $(L\text{-}HisH)_2PbBr_3I$ (**Br_3I**), $(L\text{-}HisH)_2PbBr_2I_2$ (**Br_2I_2**), $(L\text{-}HisH)_2PbBrI_3$ (**BrI_3**) and $(L\text{-}HisH)_2PbBr_{0.4}I_{3.6}$ (**$Br_{0.4}I_{3.6}$**) (where L-His = L- histidine).

According to single-crystal XRD these compounds consist of single-layered inorganic lattice with corner shared lead halide octahedra $[PbHal_4^{2-}]_\infty$ which proliferate in two dimensions and are interleaved with organic layers presented by L-histidinium(1+) cation and co-crystalized water molecules. These 2D structures result in strong quantum confinement, which leads to pronounced luminescence in the visible range.

RESULTS AND DISCUSSION

Crystal structure determination

Perovskites **I_4**, **$Br_{0.4}I_{3.6}$**, **Br_4** crystallized in form of large crystals suitable for single-crystal XRD measurements. According to single-crystal XRD perovskites **I_4** and **Br_4** crystallized in chiral space group $C222_1$ of the orthorhombic crystal system. However, in the case of **$Br_{0.4}I_{3.6}$** perovskite, the lowering of symmetry is observed. This perovskite crystallized in the chiral space group $C2$ of monoclinic family. Crystal data and structure refinement detail are summarized in Table 1.

Taking into account that the crystal structures of all obtained perovskites are very similar, only the fragments of the crystal structure of **I_4** are shown in Figure 1.

According to X-ray crystallography, the crystal structure of **I_4** is built up from anionic $[PbHal_{4/2}Hal_{2/1}^{2-}]$ inorganic framework ($Hal_{4/2}$ denotes four equatorial atoms bonded in *corner*-sharing manner and $Hal_{2/1}$ denotes two axial halogen atoms bonded only to Pb atoms), organic $L\text{-}HisH^+$ amino acid cations and co-crystallized water molecules in 2:1:0.22 ratio (Figure 1(a)). At the same time, for **Br_4** and **$Br_{0.4}I_{3.6}$** perovskites there are no co-crystallized water molecules in their crystal structures.

The central Pb^{2+} ions are coordinated with six halides forming slightly distorted $PbHal_6$ octahedron. The bond angles and bond lengths slightly deviate from ideal octahedral values (Table S1, S2). The maximum Pb−Hal bond length for **I_4**, **$Br_{0.4}I_{3.6}$** and **Br_4** is 3.2134(11) Å, 3.1872(14) Å and 3.100(3) Å, respectively. Such decrease of maximum bond length is in agreement with substitution of iodine by bromine. The same tendency is observed for the minimum Pb−Hal bond length which is 3.1496(13) Å, 3.094(6) Å and 2.953(3) Å for **I_4**, **$Br_{0.4}I_{3.6}$** and **Br_4**, respectively.

The bond angles between *cis* halogens (*cis*-Hal–Pb–Hal angles), which are helpful to assess the distortion of octahedra, vary from 82.144(15)° to 101.30(5)° for **I_4** and from 81.039(8)° to 104.86(11)° for **Br_4**. Interestingly, similar variation between the *cis*-angles is observed for **$Br_{0.4}I_{3.6}$** which change from 80.2(3)° to 98.741(8)°. Contrary to the *cis*-angles, for the *trans*-angles only slight variation of their values is observed. For example, the bond angles between *trans* halogens (*trans*-Hal–Pb–Hal angles) vary from 176.42(5)° to 177.95(5)° for **I_4** while for **Br_4** these angles vary from 174.07(12)° to 177.83(14)°. Interestingly, for **$Br_{0.4}I_{3.6}$** *trans*-angles change from 178.3(2)° to 178.6(2)°.

Table 1. Crystal data and structure refinement of **I_4**, **$Br_{0.4}I_{3.6}$** and **Br_4**

Compound	**I_4**	**$Br_{0.4}I_{3.6}$**	**Br_4**
Empirical formula	$C_{12}H_{20}N_6O_4PbI_4$ 0.22H_2O	$C_{12}H_{20}N_6O_4PbBr_{0.4}I_{3.6}$	$C_{12}H_{20}N_6O_4PbBr_4$
Fw	1031.09	1008.33	839.17
T[K]	293 K	227 K	293 K
Space group	$C222_1$	$C2$	$C222_1$
a [Å]	8.3053(15)	8.1236(9)	9.2006(6)
b [Å]	9.5330(18)	9.4686(9)	7.8434(6)
c [Å]	30.667(6)	15.3633(19)	29.935(2)
α [°]	90	90	90
β [°]	90	95.658(11)	90
γ[°]	90	90	90
V [Å^3]	2428.0(8)	1176.0(2)	2160.2(3)
Z	4	2	4
ρ_{calcd} [g·cm^{-3}]	2.821	2.848	2.580
2Θ range [°]	5.314 to 58.896	5.33 to 58.85	4.082 to 58.66
Ind. refls., R_{int}	2787, 0.0649	3232, 0.0988	2482, 0.0765
Data/restr./param.	2787/29/105	3232/74/126	2482/42/92
GOF on F^2	0.984	0.935	1.157
R_1, wR_2	0.0524, 0.0654	0.0499, 0.1054	0.0875, 0.1883
Largest diff. peak/hole [e·Å^{-3}]	1.92/−1.47	2.01/−2.00	4.70/−3.27
Flack parameter	-0.011(17)	0.04(2)	0.02(3)
CCDC No.	2207739	2207741	2207740

It worth nothing, that perovskite **$Br_{0.4}I_{3.6}$** is characterized by the lowest variation of its *trans*-angles comparing to other perovskites.

The angle distortion parameter $\Sigma = \sum_{i=1}^{12} | 90 - \alpha_i |$ (where α_i are the twelve *cis*-Hal–Pb–Hal angles around the metal atom) is often used to estimate the coordination-sphere distortion. The value of Σ for **I_4**, **$Br_{0.4}I_{3.6}$** and **Br_4** is 36.82°, 41.94° and 41.73°, respectively. It should be emphasized that **$Br_{0.4}I_{3.6}$** is characterized by the highest degree of coordination-sphere distortion among histidine-based perovskites.

Bond length distortion, $\Delta d = (1/6)\sum_{i=1}^{6}(d_i - d)^2/d^2$ (where d_i denotes the six Pb–Hal bond lengths and *d* is the mean Pb–Hal bond length), as well as bond angle variances, $\sigma^2 = \sum_{i=1}^{12}(\theta_i - 90)^2/11$ (where θ_i denotes the individual *cis*-Hal–Pb–Hal bond angles), quantify the distortions of individual $PbHal_6$ octahedra relative to an undistorted octahedron. The gradual increase of σ^2 values upon gradual substitution of iodide on bromide is observed. These values are 25.13 (°)^2, 28.63 (°)^2 and 36.04 (°)^2 for **I_4**, **$Br_{0.4}I_{3.6}$** and **Br_4**, respectively. The calculated Δd values are also gradually increasing and are $6.79\cdot10^{-5}$, $1.47\cdot10^{-4}$ and $4.10\cdot10^{-4}$ for **I_4**, **$Br_{0.4}I_{3.6}$** and **Br_4**, respectively.

As was shown previously, in-plane M–Hal–M bond angle between two adjacent *corner*-sharing octahedra (where M = Pb, Sn, *etc.*, Hal = halide anions) has the greatest impact on the tuning of the band gap of hybrid perovskites.[56] Bending the in-plane M–Hal–M bond angle away from 180°, where orbital overlap is achieved, decreases the width of the both the valence and conduction bands and increases the band gap. The in-plane Pb–Hal–Pb bond angle for **I_4** and **Br_4** is 176.42(5)° and 174.08(12)°, respectively. Interestingly, in case of **$Br_{0.4}I_{3.6}$** the in-plane Pb–Br/I–Pb bond angle is 178.3(2)°. The values of in-plane M–Hal–M bond angles for all hybrid perovskites slightly deviate from the ideal value of 180°. To the best of our knowledge, these in-plane Pb–Hal–Pb bond angles for histidine-based perovskites are among the highest for 2D hybrid perovskites.[57,58] It is important to note, that such high values of in-plane Pb–Hal–Pb bond angles for histidine-based perovskites is due to comparable sizes of imidazolium binding group (r_{eff} = 2.58 Å)[49] and cuboctahedral cavities (2.60 Å for lead iodide perovskites)[59], which leads to less distorted inorganic lattice.

Inorganic motif of all perovskites derives from cubic perovskite structure sliced along <100> direction and established by *corner*-sharing lead halide octahedra which form infinite 2D-layers. The shortest distance between adjacent inorganic layers is 15.33 Å, 15.36 Å and 14.91 Å for **I_4**, **$Br_{0.4}I_{3.6}$** and **Br_4**, respectively. The inorganic 2D-layers are interleaved by organic cation layers, which consist of protonated L-histidine molecules. The organic cations are aligned parallel to the *c*-axis. Structural analysis shows that L-histidinium cation interact with inorganic lattice both through protonated amino group and imidazolium ring. Protonated amino groups form N–H···Hal hydrogen bonds with apical halide atoms. At the same time, histidinium cations intrude into inorganic lattice and forms C–H···Hal hydrogen bonds with apical halide atoms (Figure 1(b)). Besides, in case of **I_4** the co-crystallized water molecules are engaged in

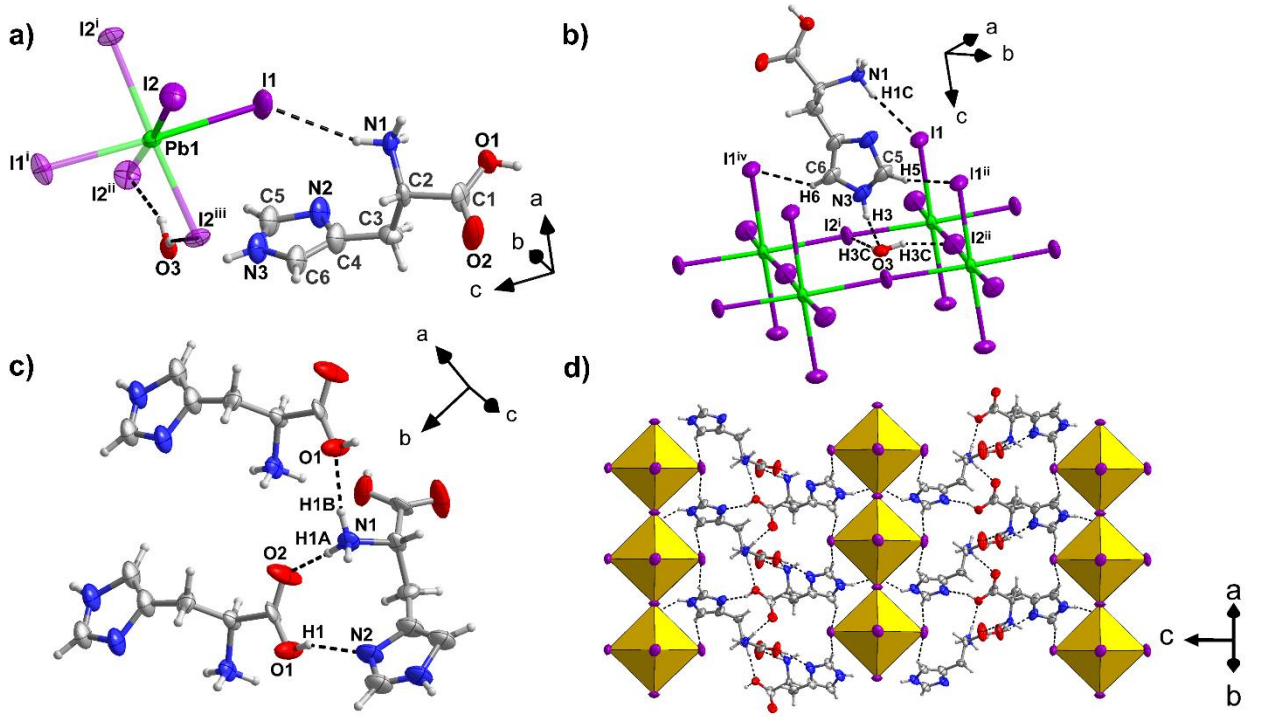

Figure 1. (a) The asymmetric unit in the crystal structure of I_4 with atom labelling scheme showing the coordination environment of the Pb atom and the organic cation. The thermal ellipsoids are drawn at the 50% probability level. **(b)** Hydrogen bonding scheme showing principal hydrogen bonds between inorganic and organic part of I_4; **(c)** Three types of hydrogen bonds inside the organic layer of I_4. **(d)** Packing diagram of I_4, showing inorganic/organic layers. The shortest distance between the adjacent inorganic layers is of 15.33 Å. Symmetry codes: i) −½+x, ½−y, 1−z; ii) −½+x, ½+y, +z; iii) +x, 1−y; 1−z; iv) −½+x, −½+y, +z.

hydrogen bonding between organic cations and inorganic lattice. Thus, water molecules interact with imidazole ring through N–H···O hydrogen bonds. In turn, water molecules bond to inorganic lattice through O–H···I hydrogen bonds with equatorial iodide atoms.

The cohesion inside the organic layers is established by three types of hydrogen bonds (Figure 1(c), Table S3). As the result, the main crystal packing motif can be characterized as a three-dimensional supramolecular network, as depicted in Figure 1(d).

The correspondence of powder samples of I_4, Br_4 to the described single crystals was confirmed by PXRD (Figure S1–S2).

Rietveld Refinement

As was previously shown, halide substitution in hybrid perovskites can progressively change their optical properties.[60] In order to demonstrate the applicability of halide substitution strategy on histidine-based hybrid perovskites, we obtained three compounds: BrI_3, Br_2I_2, Br_3I. Unfortunately, these mixed-halide perovskites do not form large crystals but precipitate as high-crystalline powders only suitable for PXRD measurements. Thus, we performed Rietveld refinement to index the crystal structure of these mixed-halide perovskites under ambient conditions. Our refinement data indicates that all mixed-halide hybrid perovskites crystallize in the monoclinic space group *C*2 with lattice parameters summarized in Table 2. A clear trend can be observed which is reduction of unit cell parameters along three principal crystallographic axes is observed with an increase of the content of bromide ions in hybrid perovskite structure (Figure 2).

Therefore, we can conclude that mixing the stoichiometric amounts of lead halide and L-histidine amino acid results in formation of hybrid mixed-halide perovskites of desirable composition. Thus, our histidine-based hybrid perovskites offer the possibility to fine tune their optoelectronic properties in wide range. Rietveld refinement data is shown in Table 2.

Rietveld refinement plots are shown in Figures S3 – S5.

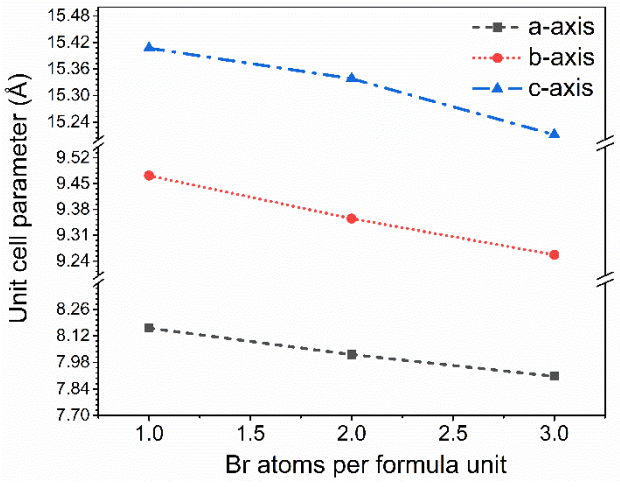

Figure 2. Dependence of unit cell parameters on Br atoms per formula unit. Reduction of unit cell parameters can be seen with an increase of Br content in all three mixed-halide hybrid perovskites.

Table 2. Crystal unit cell and Rietveld refinement data for BrI_3, Br_2I_2, Br_3I

	BrI_3	Br_2I_2	Br_3I
Temperature (K)	293	293	293
Crystal system	monoclinic	monoclinic	monoclinic
Space group	*C*2	*C*2	*C*2
a (Å)	8.1610(10)	8.0207(2)	7.9065(17)
b (Å)	9.4717(13)	9.3553(3)	9.257(2)
c (Å)	15.407(2)	15.3378(4)	15.211(3)
β (°)	95.783(9)	95.169(3)	94.745(12)
Volume (Å^3)	1184.9(3)	1146.21(6)	1109.5(4)
Z	2	2	2
R_{wp} (%)	23.125	6.714	18.038
R_p (%)	18.121	4.757	13.757

Thermogravimetric analysis

To investigate the thermal stability of these compounds at elevated temperatures, TGA measurements were conducted under nitrogen flow from 300 to 620 K (Figure 3). According to TGA measurements, compounds I_4 and Br_4 start to decompose at 445 K and 490 K, respectively (Figure 3a). The temperatures of decomposition of these hybrid perovskites are within expected range for layered 2D hybrid perovskites (Figure 3a).[61,62]Mixed-halide perovskites BrI_3, Br_2I_2 and Br_3I are losing ~1.2% of weight up to 450 K and after that temperature weight loss attains an abrupt character (Figure 3b). A multiple-step decomposition profile for all five hybrid perovskites can be observed. Unfortunately, due to strong overlay of the first and second steps of weight loss, we cannot precisely quantify the weight losses at these steps of decomposition. Therefore, any assignment of each step of weight loss to volatilization of particular component of these hybrid perovskites is difficult. However, we can assert that overall weight loss for these hybrid perovskites can be attributed to removal of water, corresponding HHal acid and partially L-histidine molecules.[63]

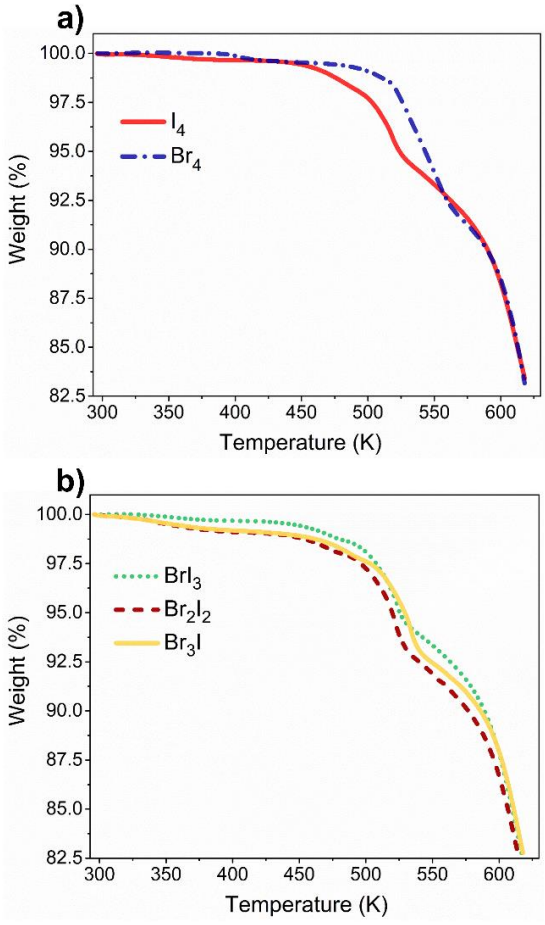

Figure 3. (a) TGA curves of compounds I_4 (red line), Br_4 (blue line); **(b)** TG curves of compounds BrI_3 (green dotted line), Br_2I_2 (brown short dashed line), Br_3I (yellow line)

OPTICAL PROPERTIES

UV-vis measurements

UV-vis measurements were performed for the bromide and iodide perovskites, but also the 1:1 perovskite to see the effect of halogen mixing. Figure 4(a) shows the solid-state UV-vis absorption spectra of compounds I_4, Br_2I_2 and Br_4 deposited on a quartz substrate measured at room temperature. It is found that there are two distinct absorption peaks in the absorption spectra of these compounds. The lower energy absorption peak finely shifts from 568 nm to 493 nm and 411 nm, respectively, upon gradual substitution of iodine on bromine (Figure 4(b)).

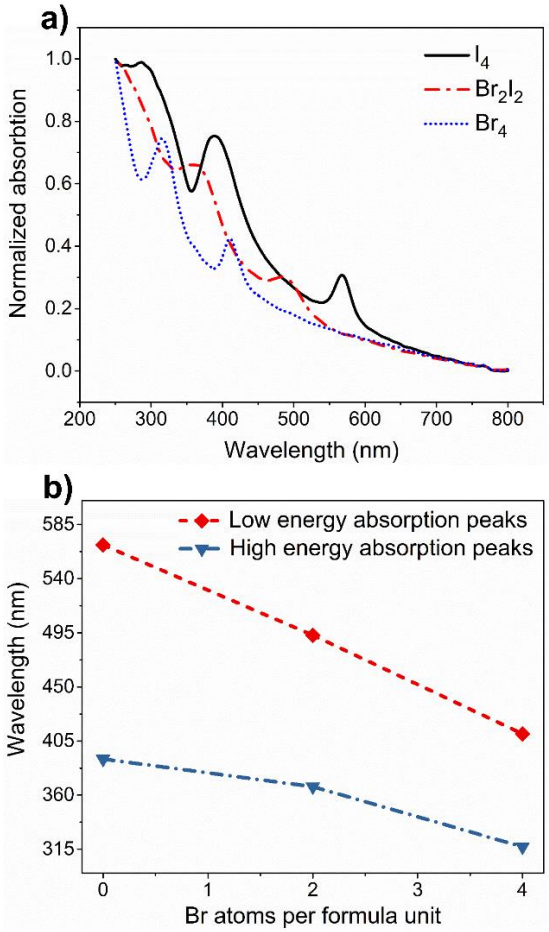

Figure 4. **(a)** UV-vis absorption spectra for compounds I_4 (blue short dot line), Br_2I_2 (red dash dot line) and I_4 (black line); **(b)** Plot demonstrating the position of the low (red dotted line) and high (blue dash dotted line) energy absorption peaks of different perovskites prepared as a function of the halide composition.

These wavelengths are, to our knowledge, the highest values observed for $PbHal_4$-based (Hal = Br, I) perovskites. In addition to the main excitonic peak, a second absorption peak is detected at 390 nm for **I_4**, 367 nm for **Br_2I_2** and 317 nm for **Br_4** (Figure 4(b)). The excitonic absorption peak at higher wavelength mainly arises from electronic transitions within the inorganic layer. Such electronic transitions occur from the top of the valence band consisting of a mixture of Pb(6s)−Hal(np) (where Hal = Br, I or Br/I, n = 4 for Br or 5 for I) states to the bottom of the conduction band consisting of the Pb(6p) state.[64,65] The absorption peaks at lower wavelength in Figure 4 are presumably attributed to both charge transfer transition between the organic and inorganic layers and higher order exciton transition energy levels.[66–69]

Photoluminescence measurements

Previous studies on various organic-inorganic lead (II) compounds has demonstrated their strong luminescence in the visible range, arising from electronic transitions within the inorganic layers. As was shown previously, hybrid perovskites incorporated imidazolium-based organic molecules are prone to exhibit strong photoluminescence.[51,70–73] Figure 5 shows the solid-state emission and excitation spectra of all five hybrid perovskites measured at room temperature.

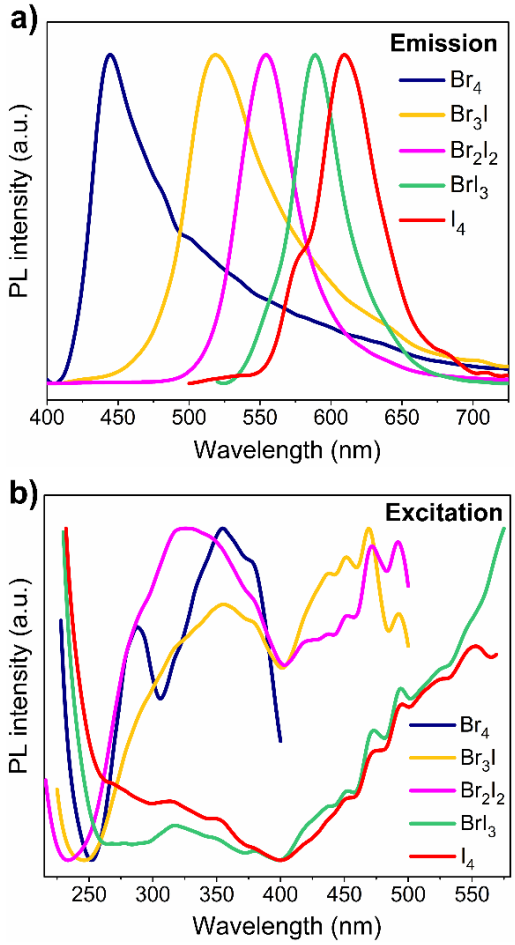

Figure 5. **(a)** Room-temperature emission spectra for solid state samples of compounds **I_4** (red line), **BrI_3** (green line), **Br_2I_2** (purple line), **Br_3I** (orange line) and **Br_4** (blue line); **(b)** room-temperature excitation spectra of **I_4** (red line), **Br_4** (blue line), **BrI_3** (green line), **Br_2I_2** (purple line), **Br_3I** (yellow line)

Table 3. Emission wavelengths (λ_{em}), FWHM and excitation wavelengths (λ_{em}) for new histidine-based hybrid perovskites.

	I_4	**BrI_3**	**Br_2I_2**	**Br_3I**	**Br_4**
Emission wavelength (λ_{em}, nm)	610 nm	589 nm	554 nm	519 nm	445 nm
FWHM (nm)	49 nm	41 nm	48 nm	73 nm	61 nm
Excitation wavelength (λ_{em}, nm)	495 nm	495 nm	350 nm	312 nm	390 nm

The photoluminescence spectra of these hybrid perovskites feature a single peak emission. The emission and excitation wavelengths for all perovskites are collected in Table 3. Considering that saturated organic molecules show no photoluminescence bands and cannot lead to the luminescence in the visible region allowed us to conclude that these bands are related to the inorganic part of these perovskites and leads to the luminescence in the visible region (Figure 5). Consequently, the observed bands are due to electronic transitions and recombination of excitons in the anionic part $[PbHal_4]^{2-}$. The photoluminescence emission spectra of all compounds show red shift as the halogen progresses from Br to I, which is consistent with previously reported results.[74] Besides, these emissions are characterized by wide full-widths at half-maximum (FWHMs) (Table 3).

These results show the perspective of histidine-based perovskites as efficient luminescent materials whose emissive properties can be readily manipulated by systematically variation of a halide ratio in the aimed perovskite. Besides, taking into account the chirality of these hybrid perovskites it is assumed that these materials may be promising for application in advanced optics and spintronics.

Conclusions

In this work, we have synthesized and characterized new chiral 2D hybrid perovskites based on the α-amino acid L-histidine. According to XRD studies, these compounds are characterized by a very similar structural motif that consists of corner-sharing lead halide octahedra arranged in <100>-oriented anion layers interleaved by organic cation layers established by monoprotonated L-histidine molecules. Importantly, histidine-based hybrid perovskites are characterized by high values of in-plane Pb–Hal–Pb bond angles, which slightly deviate from the ideal value of 180°. To the best of our knowledge, these in-plane Pb–Hal–Pb bond angles are among the highest for 2D hybrid perovskites. This shows the perspective of L-histidine of producing new hybrid perovskites with less distorted inorganic lattice that will result in a lower band gap. Interestingly, the compounds **I_4** and **Br_4** crystallized in chiral orthorhombic space group $C222_1$, whereas mixed-halide compounds **Br_3I**, **Br_2I_2** and **BrI_3** crystallized in less symmetric chiral monoclinic space group $C2$. This observation showed that halogen substitution strategy

is a promising approach not only for manipulation of optical properties of perovskites, but also for control of their crystal structures.

According to UV-vis measurements, the absorption spectra of compounds **I_4**, **Br_2I_2** and **Br_4** feature two distinct absorption peaks, which are finely blue shifted upon gradual substitution of iodine by bromine. Besides, photoluminescent measurements showed distinct halide-substituent dependent emission properties of all five perovskites, which are in good correlation with UV-vis absorption measurements. Thus, **I_4** emission is peaking at 610 nm whereas for **Br_2I_2** and **Br_4** emission maximum is observed at 554 nm and at 445 nm, respectively. These result shows that the modification over halide composition has a great impact on the optical properties of these hybrid perovskites. According to thermogravimetric analysis, the newly fabricated hybrid perovskites exhibit good thermal stability. Such stability combined with chirality and highly-tunable luminescent properties makes these materials promising for various potential applications in advanced optoelectronic and spintronic devices.

EXPERIMENTAL SECTION

Materials.

All reagents were purchased and used as received from UkrOrgSyntez Ltd. Crystals and powders used in this study were obtained via a simple solution-based method. **I_4**: PbI_2 (0.5 g, 1.08 mmol) was dissolved in the concentrated HI (57%) acid and L-histidine (0.34 g, 2.16 mmol) was then added. Small red crystals were precipitated immediately. Calcd for $C_{12}H_{20}I_4N_6O_4Pb{\cdot}H_2O$, (M = 1031.09 g mol^{-1}): C, 13.98; H, 2.00; N, 8.15%. Found: C, 13.68; H, 1.95; N, 8.05%. **BrI_3**: mixture of PbI_2 (0.15 g, 0.33 mmol) and $PbBr_2$ (0.04 g, 0.11 mmol) was dissolved in mixture of concentrated HI (57%) and HBr (48%) acids (V(HI) : V(HBr) = 3.5 : 1, 180 µL) and L-histidine (0.135 g, 0.87 mmol) was then added. Red precipitate was formed immediately. Calcd for $C_{12}H_{20}BrI_3N_6O_4Pb$, (M = 980.15 g mol^{-1}): C, 14.71; H, 2.06; N, 8.57%. Found: C, 14.59; H, 2.01; N, 8.46%. **$Br_{0.4}I_{3.6}$** (crystals): crystal of this compound was obtained as a minor by-product during the synthesis of compound **BrI_3**. **Br_2I_2**: mixture of PbI_2 (0.1 g, 0.22 mmol) and $PbBr_2$ (0.08 g, 0.22 mmol) was dissolved in mixture of concentrated HI (57%) and HBr (48%) acids (V(HI) : V(HBr) = 1.16 : 1, 160 µL) and L-histidine (0.135 g, 0.87 mmol) was the added. Orange precipitate was formed immediately. Calcd for $C_{12}H_{20}Br_2I_2N_6O_4Pb$, (M = 933.15 g mol^{-1}): C, 15.45; H, 2.16; N, 9.01%. Found: C, 15.38; H, 2.04; N, 8.92%. **Br_3I**: mixture of PbI_2 (0.05 g, 0.11 mmol) and $PbBr_2$ (0.14 g, 0.38 mmol) was dissolved in mixture of concentrated HI (57%) and HBr (48%) acids (V(HI) : V(HBr) = 1 : 3, 160 µL) and L-histidine (0.152 g, 0.98 mmol) was then added. Yellow precipitate was formed immediately. Calcd for $C_{12}H_{20}Br_3IN_6O_4Pb$, (M = 886.15 g mol^{-1}): C, 16.27; H, 2.28; N, 9.48%. Found: C, 16.19; H, 2.09; N, 9.38%. **Br_4**: $PbBr_2$ (0.5 g, 1.36 mmol) was dissolved in the concentrated HBr (48%) acid and L-histidine (0.42 g, 2.72 mmol) was then added. Pale yellow precipitate was formed immediately. Calcd for $C_{12}H_{20}Br_4N_6O_4Pb$, (M = 839.15 g mol^{-1}): C, 17.18; H, 2.40; N, 10.02%. Found: C, 17.03; H, 2.24; N, 9.89%.

Methods

The following experimental information is described in detail in the Supporting Information: elemental analyses, X-ray powder diffraction, Rietveld refinement, TGA, UV-vis, PL, X-ray structure determination.

Author Contributions

The manuscript was written through contributions of all authors. All authors have given approval to the final version of the manuscript.

Conflicts of interest

There are no conflicts to declare.

Acknowledgements

Authors acknowledge the financial support from the Ministry of Education and Science of Ukraine (grant No. 22BF037-09), and the research infrastructure developed through the European Social Fund for Regional Development, Competitiveness Operational Programme 2014-2020, Axis 1, Action: 1.1.3, Project “Infra SupraChem Lab - Center for Advanced Research in Supramolecular Chemistry” (Contract 339/390015/25.02.2021, cod MySMIS: 108983). Authors also aknowladge the courage of the Armed Forces of Ukraine that made the submission of this manuscript possible.

Notes and references

1 Z. Xiao, R. A. Kerner, L. Zhao, N. L. Tran, K. M. Lee, T.-W. Koh, G. D. Scholes and B. P. Rand, *Nat. Photonics*, 2017, **11**, 108–115.

2 Z. Tan, Y. Wu, H. Hong, J. Yin, J. Zhang, L. Lin, M. Wang, X. Sun, L. Sun, Y. Huang, K. Liu, Z. Liu and H. Peng, *J. Am. Chem. Soc.*, 2016, **138**, 16612–16615.

3 P. Li, Y. Chen, T. Yang, Z. Wang, H. Lin, Y. Xu, L. Li, H. Mu, B. N. Shivananju, Y. Zhang, Q. Zhang, A. Pan, S. Li, D. Tang, B. Jia, H. Zhang and Q. Bao, *ACS Appl. Mater. Interfaces*, 2017, **9**, 12759–12765.

4 W. Mao, J. Zheng, Y. Zhang, A. S. R. Chesman, Q. Ou, J. Hicks, F. Li, Z. Wang, B. Graystone, T. D. M. Bell, M. U. Rothmann, N. W. Duffy, L. Spiccia, Y. Cheng, Q. Bao and U. Bach, *Angew. Chemie*, 2017, **129**, 12660–12665.

5 Y. Zhang, C. K. Lim, Z. Dai, G. Yu, J. W. Haus, H. Zhang and P. N. Prasad, *Phys. Rep.*, 2019, **795**, 1–51.

6 G. Long, C. Jiang, R. Sabatini, Z. Yang, M. Wei, L. N. Quan, Q. Liang, A. Rasmita, M. Askerka, G. Walters, X. Gong, J. Xing, X. Wen, R. Quintero-Bermudez, H. Yuan, G. Xing, X. R. Wang, D. Song, O. Voznyy, M. Zhang, S. Hoogland, W. Gao, Q. Xiong and E. H. Sargent, *Nat. Photonics*, 2018, **12**, 528–

533.
7 N. J. Jeon, J. H. Noh, W. S. Yang, Y. C. Kim, S. Ryu, J. Seo and S. Il Seok, *Nature*, 2015, **517**, 476–480.
8 W. S. Yang, B.-W. Park, E. H. Jung, N. J. Jeon, Y. C. Kim, D. U. Lee, S. S. Shin, J. Seo, E. K. Kim, J. H. Noh and S. Il Seok, *Science*, 2017, **356**, 1376–1379.
9 D. P. McMeekin, G. Sadoughi, W. Rehman, G. E. Eperon, M. Saliba, M. T. Hörantner, A. Haghighirad, N. Sakai, L. Korte, B. Rech, M. B. Johnston, L. M. Herz and H. J. Snaith, *Science*, 2016, **351**, 151–5.
10 Y. Il Lee, N. J. Jeon, B. J. Kim, H. Shim, T.-Y. Yang, S. Il Seok, J. Seo and S. G. Im, *Adv. Energy Mater.*, 2018, **8**, 1701928.
11 W. S. Yang, J. H. Noh, N. J. Jeon, Y. C. Kim, S. Ryu, J. Seo and S. Il Seok, *Science*, 2015, **348**, 1234–7.
12 A. Kojima, K. Teshima, Y. Shirai and T. Miyasaka, *J. Am. Chem. Soc.*, 2009, **131**, 6050–1.
13 NREL, Best Research-Cell Efficiency Chart, https://www.nrel.gov/pv/cell-efficiency.html, (accessed 13 June 2022).
14 G. E. Eperon, S. D. Stranks, C. Menelaou, M. B. Johnston, L. M. Herz and H. J. Snaith, *Energy Environ. Sci.*, 2014, **7**, 982.
15 M. M. Lee, J. Teuscher, T. Miyasaka, T. N. Murakami and H. J. Snaith, *Science*, 2012, **338**, 643–7.
16 S. D. Stranks, G. E. Eperon, G. Grancini, C. Menelaou, M. J. P. Alcocer, T. Leijtens, L. M. Herz, A. Petrozza and H. J. Snaith, *Science*, 2013, **342**, 341–4.
17 G. Giorgi, J. Fujisawa, H. Segawa and K. Yamashita, *J. Phys. Chem. C*, 2014, **118**, 12176–12183.
18 W.-J. Yin, T. Shi and Y. Yan, *Adv. Mater.*, 2014, **26**, 4653–4658.
19 Y. Yang, J. You, Z. Hong, Q. Chen, M. Cai, T. Bin Song, C. C. Chen, S. Lu, Y. Liu and H. Zhou, *ACS Nano*, 2014, **8**, 1674–1680.
20 D. Weber, *Zeitschrift für Naturforsch. B*, 1978, **33**, 1443–1445.
21 D. Weber, *Zeitschrift für Naturforsch. B*, 1978, **33**, 862–865.
22 D. B. Mitzi and K. Liang, *J. Solid State Chem.*, 1997, **134**, 376–381.
23 C. C. Stoumpos, C. D. Malliakas and M. G. Kanatzidis, *Inorg. Chem.*, 2013, **52**, 9019–9038.
24 H. R. Petrosova, O. I. Kucheriv, S. Shova and I. A. Gural'skiy, *Chem. Commun.*, 2022, **58**, 5745–5748.
25 M. Mączka, M. Ptak, A. Gągor, D. Stefańska, J. K. Zaręba and A. Sieradzki, *Chem. Mater.*, 2020, **32**, 1667–1673.
26 M. Mączka, A. Gagor, J. K. Zaręba, D. Stefanska, M. Drozd, S. Balciunas, M. Šimėnas, J. Banys and A. Sieradzki, *Chem. Mater.*, 2020, **32**, 4072–4082.
27 D. Drozdowski, A. Gągor, D. Stefańska, J. K. Zaręba, K. Fedoruk, M. Mączka and A. Sieradzki, *J. Phys. Chem. C*, 2022, **126**, 1600–1610.
28 Z. Xiao, K.-Z. Du, W. Meng, J. Wang, D. B. Mitzi and Y. Yan, *J. Am. Chem. Soc.*, 2017, **139**, 6054–6057.
29 T. Leijtens, G. E. Eperon, N. K. Noel, S. N. Habisreutinger, A. Petrozza and H. J. Snaith, *Adv. Energy Mater.*, 2015, **5**, 1–23.
30 L. Mao, C. C. Stoumpos and M. G. Kanatzidis, *J. Am. Chem. Soc.*, 2019, **141**, 1171–1190.
31 T. Zhu and X. Gong, *InfoMat*, 2021, 3, 1039–1069.
32 T. Sheikh, S. Maqbool, P. Mandal and A. Nag, *Angew. Chemie - Int. Ed.*, 2021, **60**, 18265–18271.
33 D. B. Mitzi, *J. Chem. Soc. Dalt. Trans.*, 2001, 1–12.
34 M. Bokdam, T. Sander, A. Stroppa, S. Picozzi, D. D. Sarma, C. Franchini and G. Kresse, *Sci. Rep.*, 2016, **6**, 28618.
35 C. Lee, J. Hong, A. Stroppa, M.-H. Whangbo and J. H. Shim, *RSC Adv.*, 2015, **5**, 78701–78707.
36 R. C. Remsing and M. L. Klein, *APL Mater.*, 2020, **8**, 050902.
37 C. Yang, W. Chen, Y. Ding, J. Wang, Y. Rao, W. Liao, Y. Tang, P. Li, Z. Wang and R. Xiong, *Adv. Mater.*, 2019, **31**, 1808088.
38 Y. Ai, X.-G. Chen, P.-P. Shi, Y.-Y. Tang, P.-F. Li, W.-Q. Liao and R.-G. Xiong, *J. Am. Chem. Soc.*, 2019, **141**, 4474–4479.
39 Y. Liu, L. Collins, R. Proksch, S. Kim, B. R. Watson, B. Doughty, T. R. Calhoun, M. Ahmadi, A. V. Ievlev, S. Jesse, S. T. Retterer, A. Belianinov, K. Xiao, J. Huang, B. G. Sumpter, S. V. Kalinin, B. Hu and O. S. Ovchinnikova, *Nat. Mater.*, 2018, **17**, 1013–1019.
40 K. Mencel, V. Kinzhybalo, R. Jakubas, J. K. Zaręba, P. Szklarz, P. Durlak, M. Drozd and A. Piecha-Bisiorek, *Chem. Mater.*, 2021, **33**, 8591–8601.
41 C. Yuan, X. Li, S. Semin, Y. Feng, T. Rasing and J. Xu, *Nano Lett.*, 2018, **18**, 5411–5417.
42 J. Ahn, E. Lee, J. Tan, W. Yang, B. Kim and J. Moon, *Mater. Horizons*, 2017, **4**, 851–856.
43 J. Ahn, S. Ma, J. Y. Kim, J. Kyhm, W. Yang, J. A. Lim, N. A. Kotov and J. Moon, *J. Am. Chem. Soc.*, 2020, **142**, 4206–4212.
44 J. Ma, C. Fang, C. Chen, L. Jin, J. Wang, S. Wang, J. Tang and D. Li, *ACS Nano*, 2019, **13**, 3659–3665.
45 H. Huang, *Nat. Photonics*, 2010, **4**, 134–135.
46 M. Ben Haj Salah, N. Mercier, M. Allain, N. Zouari and C. Botta, *J. Mater. Chem. C*, 2019, **7**, 4424–4433.
47 V. Y. Sirenko, O. I. Kucheriv, D. D. Naumova, I. V. Fesych, R. P. Linnik, I.-A. Dascălu, S. Shova, I. O. Fritsky and I. A. Gural'skiy, *New J. Chem.*, 2021, **45**, 12606–12612.
48 J. Cheng, Y. Deng, X. Dong, J. Li, L. Huang, H. Zeng, G. Zou and Z. Lin, *Inorg. Chem.*, 2022, **61**, 11032–11035.
49 G. Kieslich, S. Sun and A. K. Cheetham, *Chem. Sci.*, 2014, **5**, 4712–4715.
50 Y. Li, T. Yang, X. Liu, S. Han, J. Wang, Y. Ma, W. Guo, J. Luo and Z. Sun, *Inorg. Chem. Front.*, 2020, **7**, 2770–2777.
51 L. Mao, H. Tsai, W. Nie, L. Ma, J. Im, C. C. Stoumpos, C. D. Malliakas, F. Hao, M. R. Wasielewski, A. D. Mohite and M. G. Kanatzidis, *Chem. Mater.*, 2016, **28**, 7781–7792.
52 B. Febriansyah, T. M. Koh, Y. Lekina, N. F. Jamaludin, A. Bruno, R. Ganguly, Z. X. Shen, S. G. Mhaisalkar and J. England, *Chem. Mater.*, 2019, **31**, 890–898.
53 W. Seo and K. M. Ok, *Inorg. Chem. Front.*, 2021, **8**, 4536–4543.
54 H. Choi and K. M. Ok, *Inorg. Chem. Front.*, 2021, **8**, 3843–3850.
55 A. Tofanello, A. L. M. Freitas, T. B. de Queiroz, A. Bonadio, H. Martinho and J. A. Souza, *J. Phys. Chem. Lett.*, 2022, **13**, 1406–1415.
56 J. L. Knutson, J. D. Martin and D. B. Mitzi, *Inorg. Chem.*,

2005, **44**, 4699–4705.
57 K. Z. Du, Q. Tu, X. Zhang, Q. Han, J. Liu, S. Zauscher and D. B. Mitzi, *Inorg. Chem.*, 2017, **56**, 9291–9302.
58 M. D. Smith, A. Jaffe, E. R. Dohner, A. M. Lindenberg and H. I. Karunadasa, *Chem. Sci.*, 2017, **8**, 4497–4504.
59 D. B. Mitzi, *J. Chem. Soc. Dalt. Trans.*, 2001, 1–12.
60 A. Zanetta, Z. Andaji-Garmaroudi, V. Pirota, G. Pica, F. U. Kosasih, L. Gouda, K. Frohna, C. Ducati, F. Doria, S. D. Stranks and G. Grancini, *Adv. Mater.*, 2022, **34**, 2105942.
61 S. K. Yu, Z. R. Zhang, Z. H. Ren, H. L. Zhai, Q. Y. Zhu and J. Dai, *Inorg. Chem.*, 2021, **60**, 9132–9140.
62 Y. Zhang, Y. Liu, Z. Xu, H. Ye, Q. Li, M. Hu, Z. Yang and S. (Frank) Liu, *J. Mater. Chem. C*, 2019, **7**, 1584–1591.
63 D. B. Mitzi, *Chem. Mater.*, 1996, **8**, 791–800.
64 K. Du, Q. Tu, X. Zhang, Q. Han, J. Liu, S. Zauscher and D. B. Mitzi, *Inorg. Chem.*, 2017, **56**, 9291–9302.
65 S. Zhang, P. Audebert, Y. Wei, A. Al Choueiry, G. Lanty, A. Bréhier, L. Galmiche, G. Clavier, C. Boissière, J.-S. Lauret and E. Deleporte, *Materials (Basel).*, 2010, **3**, 3385–3406.
66 G. Vijaya Prakash, K. Pradeesh, R. Ratnani, K. Saraswat, M. E. Light and J. J. Baumberg, *J. Phys. D. Appl. Phys.*, 2009, **42**, 185405.
67 K. Pradeesh, K. Nageswara Rao and G. Vijaya Prakash, *J. Appl. Phys.*, 2013, **113**, 083523.
68 E. R. Dohner, A. Jaffe, L. R. Bradshaw and H. I. Karunadasa, *J. Am. Chem. Soc.*, 2014, **136**, 13154–13157.
69 Y. Li, G. Zheng, C. Lin and J. Lin, *Cryst. Growth Des.*, 2008, **8**, 1990–1996.
70 Y. Li, C. Lin, G. Zheng and J. Lin, *J. Solid State Chem.*, 2007, **180**, 173–179.
71 B. Febriansyah, D. Giovanni, S. Ramesh, T. M. Koh, Y. Li, T. C. Sum, N. Mathews and J. England, *J. Mater. Chem. C*, 2020, **8**, 889–893.
72 Z. Wu, C. Ji, Z. Sun, S. Wang, S. Zhao, W. Zhang, L. Li and J. Luo, *J. Mater. Chem. C*, 2018, **6**, 1171–1175.
73 S.-S. Yu, S.-X. Jiang, H. Zhang and H.-B. Duan, *Inorg. Chem. Commun.*, 2020, **112**, 107690.
74 A. García-Fernández, I. Marcos-Cives, C. Platas-Iglesias, S. Castro-García, D. Vázquez-García, A. Fernández and M. Sánchez-Andújar, *Inorg. Chem.*, 2018, **57**, 7655–7664.